



CHALMERS
UNIVERSITY OF TECHNOLOGY

Dynamical Excitation Control and Multimode Emission of an Atom-Photon Bound State

Downloaded from: <https://research.chalmers.se>, 2025-04-20 06:37 UTC

Citation for the original published paper (version of record):

Castillo-Moreno, C., Rafsanjani Amin, K., Strandberg, I. et al (2025). Dynamical Excitation Control and Multimode Emission of an Atom-Photon Bound State. *Physical Review Letters*, 134(13).
<http://dx.doi.org/10.1103/PhysRevLett.134.133601>

N.B. When citing this work, cite the original published paper.

Dynamical Excitation Control and Multimode Emission of an Atom-Photon Bound StateClaudia Castillo-Moreno¹,* Kazi Rafsanjani Amin¹, Ingrid Strandberg¹,Mikael Kervinen,[†] Amr Osman¹, and Simone Gasparinetti^{1,‡}*Department of Microtechnology and Nanoscience, Chalmers University of Technology, 412 96 Gothenburg, Sweden* (Received 16 April 2024; revised 17 January 2025; accepted 25 February 2025; published 31 March 2025)

Atom-photon bound states arise from the coupling of quantum emitters to the band edge of dispersion-engineered waveguides. Thanks to their tunable-range interactions, they are promising building blocks for quantum simulators. Here, we study the dynamics of an atom-photon bound state emerging from coupling a frequency-tunable quantum emitter—a transmon-type superconducting circuit—to the band edge of a microwave metamaterial. Employing precise temporal control over the frequency detuning of the emitter from the band edge, we examine the transition from adiabatic to nonadiabatic behavior in the formation of the bound state and its melting into the propagating modes of the metamaterial. Moreover, we experimentally observe multimode emission from the bound state, triggered by a fast change of the emitter’s frequency. Our Letter offers insight into the dynamic preparation of APBS and provides a method to characterize their photonic content, with implications in quantum optics and quantum simulation.

DOI: [10.1103/PhysRevLett.134.133601](https://doi.org/10.1103/PhysRevLett.134.133601)

Coupling quantum emitters to photonic lattices or metamaterials strongly modifies their spontaneous emission. When the emitter’s frequency is close to a band edge and within a band gap of the lattice, an atom-photon bound state (APBS) is formed—a stationary excitation whose photonic component is exponentially localized around the physical location of the emitter. Because the localization length is controlled by the frequency detuning from the band edge, APBS can mediate long-distance interactions with tunable range [1]. Following theoretical studies [1–13], APBS have been observed in ultracold atoms coupled to photonic waveguides, optical lattices, and superconducting circuits [14–23], and their properties have been leveraged to simulate spin models, prepare many-body correlated states, and explore many-body quantum phase transitions [19,24–29].

Despite these advances, a dynamical characterization of individual atom-photon-bound states is still lacking. The (static) exponential localization of the photonic component has been characterized through their interaction with the metamaterial edges or among APBS clouds [30–32], or by coupling emitters to each resonator site [26,33]. Additionally, time-dependent studies have observed non-

Markovian dynamics [34], population exchanges [35], and photonic hoppings through the metamaterial [26]. These measurements involve fast “quenches” in which the photonic fraction of the APBS, as well as its localization length, are rapidly changed by varying the frequency of the emitter. Yet, the detailed dynamics, characteristic timing, and mode decomposition of these states remain unexamined.

In this Letter, we study the time-dependent formation and melting of an APBS in a superconducting circuit. We combine dispersive measurements of the atomic population with frequency-resolved measurements of the radiation emitted by the APBS as the emitter is quenched. After the quench, the photonic part of the APBS, which was localized when the APBS was formed, turns into delocalized states in the metamaterial which then propagate and are measured at the output of our metamaterial. We refer to this process as “melting.” We observe a crossover from adiabatic to nonadiabatic dynamics due to multistate Landau-Zener tunneling to the frequency modes at the band edge of the photonic band. Moreover, we characterize the emitted radiation when quenching the APBS and detect multimode emission from up to nine modes of the metamaterial. We find that an effective model captures overall trends, but precise dynamics and emission’s spectral content are very sensitive to disorder in the metamaterial. Our methodology is generally applicable to localized excitations of emitters coupled to photonic lattices and can facilitate the design of quantum simulators [1,26,27] and topological interconnects [36].

Our superconducting quantum circuit includes a metamaterial consisting of an array of 21 nearest-neighbor-coupled, lumped-element resonators [Fig. 1(a)]. Each resonator features an array of ten Josephson junctions as

*Contact author: claudiac@chalmers.se[†]Present address: VTT Technical Research Centre of Finland Ltd. Tietotie 3, Espoo 02150, Finland.[‡]Contact author: simoneg@chalmers.se

Published by the American Physical Society under the terms of the Creative Commons Attribution 4.0 International license. Further distribution of this work must maintain attribution to the author(s) and the published article’s title, journal citation, and DOI. Funded by Bibsam.

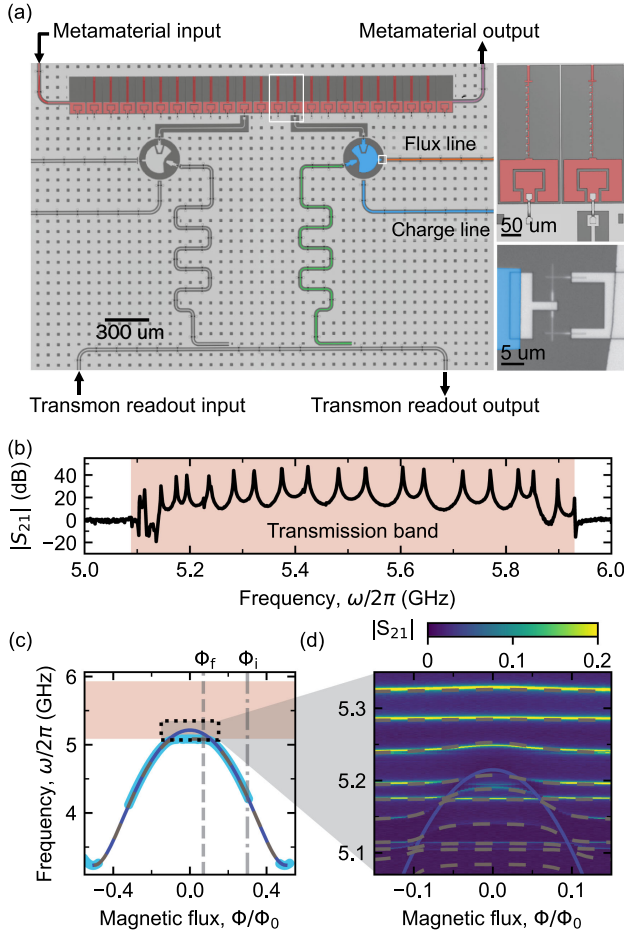


FIG. 1. Quantum emitter coupled to a metamaterial. (a) False-color micrograph of the device. Salmon: lumped-element resonator array forming the metamaterial. Blue: transmon. Green: readout resonator. Insets, in white, show (top) two resonators including the Josephson junction arrays, and (bottom) transmon's SQUID. (b) $|S_{21}|$ vs frequency. Transmission band in salmon. (c) Emitter frequency vs magnetic flux. Light blue: APBS frequency. Dark blue: bare emitter frequency. Gray, dashed: APBS frequency from the effective model. Vertical gridlines illustrative working points. (d) $|S_{21}|$ vs flux and frequency, with the response of the nine first metamaterial modes to a change in the bare emitter frequency (dark blue). Dashed lines: model.

the inductor, shunted by a capacitive element, resulting in a characteristic impedance $Z_r \approx 390\Omega$ [35]. Input and output ports are capacitively coupled to the metamaterial's first and last sites to directly measure its transmission band and collect emitted radiation from the system. Two frequency-tunable, transmon-type artificial atoms [37,38] are capacitively coupled to the metamaterial resonators at sites 10 and 13. The two transmons are nominally identical and use asymmetric superconducting quantum interference devices (SQUIDs) as nonlinear inductors, resulting in two first-order flux insensitive points (sweet spots). The lower one resides well below the metamaterial's photonic band and the upper one inside it. Dedicated lines allow precise

control of the transmon's frequency, via the flux (Z control), and population excitation, through the charge (XY control), while dispersively coupled, frequency-multiplexed readout resonators allow measurement of the transmon populations [39]. In the following, we use the transmon coupled to site 13 [false-colored in blue in Fig. 1(a)] as a quantum emitter, while the other is kept at its lower sweet spot and does not participate in the presented experiments (see Supplemental Material [48]).

We characterize the metamaterial by measuring the transmission coefficient, $|S_{21}|$, while keeping the emitter far detuned from the transmission band, $\Phi/\Phi_0 = 0.5$. This measurement reveals a transmission band between 5.088 and 5.93 GHz composed of 21 modes (detected as peaks), corresponding to the (hybridized) 21 resonators [Fig. 1(b)]. A tight-binding description of the system, assuming identical resonators of frequency ω_r and nearest-neighbor coupling J , predicts a transmission band in the frequency range $[\omega_r - 2J, \omega_r + 2J]$. Fitting this expression to the data, we extract $\omega_r/2\pi \approx 5.5$ GHz and $J/2\pi \approx 211$ MHz. However, mode spacing and linewidths significantly deviate from the tight-binding prediction, a previously reported effect [35] that we ascribe to disorder in the resonators.

To characterize the interaction of the emitter with the metamaterial, we sweep its bare frequency via the flux applied through the SQUID, Φ , and measure its dressed frequency with two-tone spectroscopy [Fig. 1(c)]. Far from the photonic band, the data points follow the usual flux dependence of asymmetric transmons [40]. Near the band edge, interactions with metamaterial modes cause deviations: the emitter frequency is prevented from entering the transmission band, signaling the formation of an APBS at the lower band edge [5] [Fig. 1(c)], and, the frequency of several modes in the band gets shifted, interpreted as due to multimode strong coupling in a finite-bandwidth waveguide [31] [Fig. 1(d)].

Metamaterial frequencies and their interaction with the emitter are sensitive to circuit disorder; therefore, an identical-resonators model cannot quantitatively reproduce them. To make contact with the spectroscopy data and model subsequent experiments, we use a model with the band's mode frequencies and their individual couplings to the emitter as free parameters.

This effective model is described by the Hamiltonian

$$H = \sum_{n=1}^N \tilde{\omega}_n a_n^\dagger a_n + \omega_q(\Phi) \frac{\sigma_z}{2} + \sum_{n=1}^N g_n (a_n \sigma_+ + a_n^\dagger \sigma_-), \quad (1)$$

in which $\tilde{\omega}_n$ are the dressed frequencies of the photonic modes, a_n (a_n^\dagger) are their corresponding photon annihilation (creation) operators, $\omega_q(\Phi)$ is the flux-dependent emitter frequency, and g_n the static couplings between the emitter and each photonic mode. We truncate the Hamiltonian to the single-excitation subspace (Supplemental Material [48]). Additionally, we focus on the first $N = 9$ modes

from the lower band edge, as the remaining ones do not show appreciable frequency shift when the emitter frequency is changed [Fig. 1(d)]. Our model reproduces the spectroscopy data when using mode frequencies extracted from measurements with the emitter far detuned and best-fitted coupling strengths $g_n/2\pi = 3\text{--}25$ MHz.

The emitter and the metamaterial interaction gives rise to an APBS, which consists of a superposition of an emitterlike and a photonlike excitation, mathematically defined as

$$|\Psi_{\text{APBS}}\rangle = c_E \sigma_+ |g, 0\rangle + \sum_{i=1}^N c_i a_i^\dagger |g, 0\rangle, \quad (2)$$

in which c_E (c_i) is the amplitude coefficient of the emitterlike (i th photonlike) state, $|g, 0\rangle$ is the ground state of the composite system, σ_+ the ladder operator, and a_i^\dagger the creation operator [5]. The probability coefficients depend on the detuning between the emitter and the band. Therefore, by manipulating ω_q through Φ , we can study the formation and melting of the APBS between two points, an emitterlike point, Φ_i , at which the emitter is away from the band-edge and the APBS responds as a two-level system, and a photonlike point, Φ_f , at which the emitter is highly hybridized with the photonic band [41] [Fig. 1(c)].

APBS dynamics are explored by transitioning between these points at different speeds [Fig. 2(a)]. Starting at Φ_i , we excite the emitter with a π pulse. Then, we apply a trapezoid-shaped flux pulse between Φ_i and Φ_f , characterized by a rise time $\tau_r=10\text{--}200$ ns, a hold time $\tau_{\text{hold}} = 0\text{--}400$ ns, and a fall time $\tau_f=10\text{--}200$ ns. After returning to Φ_i , we measure the remaining population in the emitter, $P_{|1\rangle}$, as a function of the time spent in Φ_f for varying τ_r and τ_f [Fig. 2(b)]. To remove the effect of decoherence, we interleave each measurement with a reference taken without the flux pulse, keeping the time delay constant.

As τ_r and τ_f decrease, $P_{|1\rangle}$ decreases on average and oscillates with an increasing number of frequency components, as confirmed by a fast-Fourier transform (FFT) of $P_{|1\rangle}$ [Fig. 2(c)]. For $\tau_r = \tau_f = 200$ ns, $P_{|1\rangle}$ is largely restored without oscillation. For $\tau_r = \tau_f = 50$ ns, average $P_{|1\rangle}$ decreases, and reproducible oscillations appear, as evident from FFT. For even shorter $\tau_r = \tau_f = 10$ ns, $P_{|1\rangle}$ decreases further, and more frequency components appear in the oscillations.

To understand these trends, we solve the time-dependent Schrödinger equation of the Hamiltonian in Eq. (1), incorporating the time-dependent ω_q from the applied flux pulse and flux-to-frequency transfer function. Our model qualitatively reproduces the observed behavior, with decreasing population and increasing oscillations as the formation and melting speeds increase [Figs. 2(d) and 2(e)].

In both the measurement and the simulation, oscillation frequencies align with differences between the system's dressed modes [Figs. 2(c) and 2(e)]. This correspondence

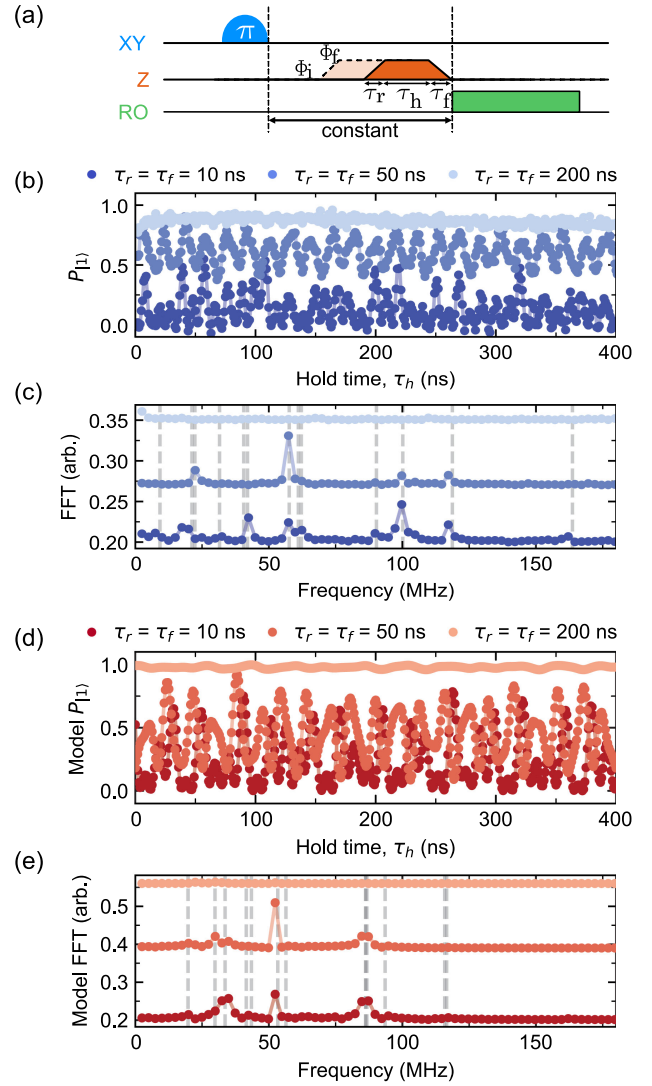


FIG. 2. APBS formation and melting at different speeds at $\omega_q(\Phi_f) \approx 5.2$ GHz. (a) Pulse sequence. (b) Transmon population vs hold time for $\tau_r = \tau_f = 10, 50, 200$ ns. (c) FFT of (b). Data shifted vertically for clarity. Dashed lines correspond to the frequency differences between the modes at Φ_f . (d),(e) Simulation results for (b),(c).

suggests that the coupling between the APBS and the metamaterial modes enables a non-zero probability of population transitions from one mode to the other, by Landau-Zener tunneling [42–45]. Therefore, for short τ_r/τ_f , the emitter's excitation gets distributed over several modes, with beatings in the emitter population due to quantum interference.

In contrast, for long τ_r/τ_f , the large $P_{|1\rangle}$ and the lack of oscillations indicate the population is adiabatically transferred to the APBS. The threshold for adiabatic transfer depends on the mode frequencies and their coupling strength, and it is coarsely estimated from the single-mode Landau-Zener formula, $P_{\text{LZ}} = \exp(-2\pi\Gamma)$, with $\Gamma = g^2\Delta t/\Delta E$, in which ΔE is the difference between

the emitter's initial and final energies, Δt the τ_r , and g coupling between the emitter and each metamaterial mode. Our estimates show the adiabatic limit is reached for $\Delta t = 200\text{--}300$ ns, matching observations.

However, the model and data show two quantitative differences. While the model predicts $P_{|1\rangle} = 1$ for $\tau_r = \tau_f = 200$ ns, the data shows $P_{|1\rangle} = 0.9$. We attribute this difference to population transfer to a coherent two-level system with a resonant frequency between $\omega_q(\Phi_i)$ and $\omega_q(\Phi_f)$ (Supplemental Material [48]). Additionally, FFT peak frequencies and intensities do not exactly match [Figs. 2(d) and 2(e)], possibly from an incorrect model-parameter estimate from the spectroscopy data or the uncorrected flux-line transfer function [46].

The demonstrated dynamic control enables direct access to the APBS's photonic component by melting the APBS following a quench. To do so, we adiabatically prepare the APBS by exciting the emitter with a $\pi/2$ pulse and then slowly ramping Φ between Φ_i and Φ_f . $\tau_{\text{hold}} = 40$ ns for stabilization. Then, we quickly ramp Φ back to Φ_i . At the same time, we record the coherent component, $\langle \hat{a}_{\text{out}} \rangle$, of the outgoing field from the output port of the metamaterial, for $20 \mu\text{s}$ [Fig. 3(a)].

The time trace [Fig. 3(b)] is digitally recorded with a 1-GHz-wide acquisition band centered at 5 GHz. Its FFT reveals a total of nine prominent peaks [Fig. 3(c)]. Notably, the frequencies of the peaks show a one-to-one correspondence with the frequencies of the 9 metamaterials's lowest-frequency modes [Fig. 1(b)]. We extract the temporal envelope of the radiation emitted into each mode by demodulating the time trace at each of the peak frequencies [selected traces in Fig. 3(d)]. The emission from each mode decays exponentially with a distinct decay rate [Fig. 3(e)] (Supplemental Material [48]). As a general trend, the decay rates are slower near the band edge and become faster toward the center of the band. This arises from states near the band edge having a group velocity that approaches zero, and, therefore, they interact less with the boundaries of the metamaterial [5,35] (Supplemental Material [48]). Additionally, a good agreement exists between our values and those predicted by the tight-binding model [Fig. 3(e)]. We quantify the emitted photons in each mode by integrating $\langle \hat{a}_n \rangle$ and squaring the result [Fig. 3(f)].

A quench in emitter frequency traps populations in the prequench instantaneous eigenstates. Subsequently, the photonic population is converted into propagating photonic modes in the metamaterial that decay to the output port. Therefore, we interpret this measurement as a decomposition of the APBS's photonic part, providing a quantitative estimate of the relative probability densities in Eq. (2). Because the multimode emission stems from a single excitation in the APBS, we expect these modes to be entangled. However, a detailed study of the mode correlations is reserved for future research.

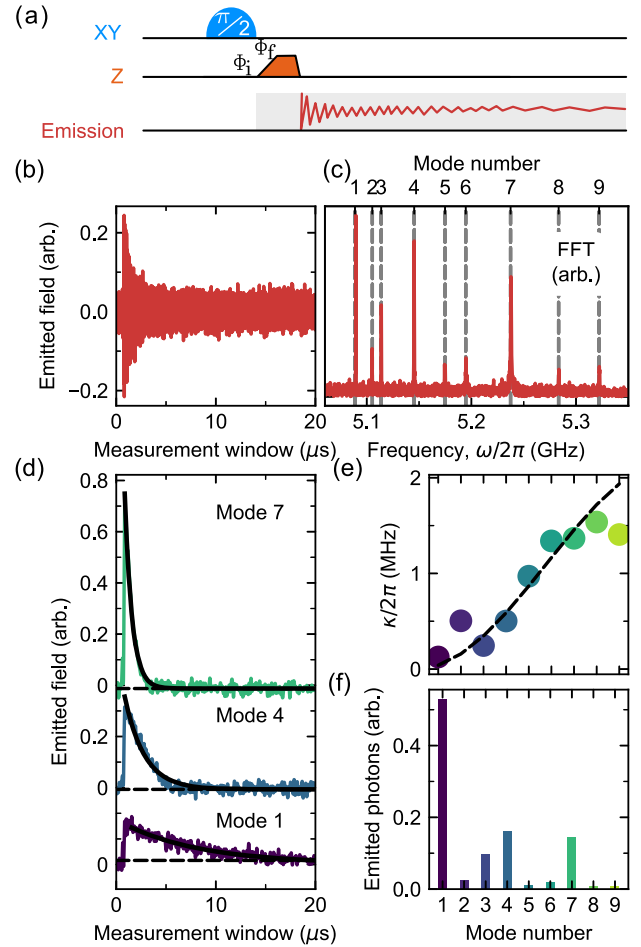


FIG. 3. Multimode emission at $\omega_q(\Phi_f) \approx 5.2$ GHz. (a) Pulse sequence. (b) Time trace of the emitted field. (c) FFT of (b). Vertical gridlines: metamaterial modes frequencies, extracted from Fig. 1(d). (d) Demodulated time traces for selected modes with exponential fits (black lines). (e) Filled circles: emission decay rates vs mode index, extracted from fits in (d); dashed lines: tight-binding model predictions. (f) Emitted photons vs mode index.

We further explore the spectrally resolved emission of the APBS by varying the conditions for its formation. For different Φ_f in the adiabatic regime, the emission mirrors the decomposition of the photonic component of the APBS. Far from the band, the APBS is in the emitterlike state and the emission is weak. Once the frequency approaches the band edge, the APBS becomes more photoniclike, and emission, mainly from the first mode, increases until it saturates. The contribution of higher-frequency modes depends on the specific realization of disorder in the array and varies nonmonotonically when approaching the band edge and rapidly increases once within the band with Φ_f [Fig. 4(a)].

The effect of τ_r near the band edge reveals a transition from single-mode to multimode emission with a sharp rise in the contribution of higher-frequency modes as τ_r decreases [Fig. 4(a)]. We interpret this behavior as a direct

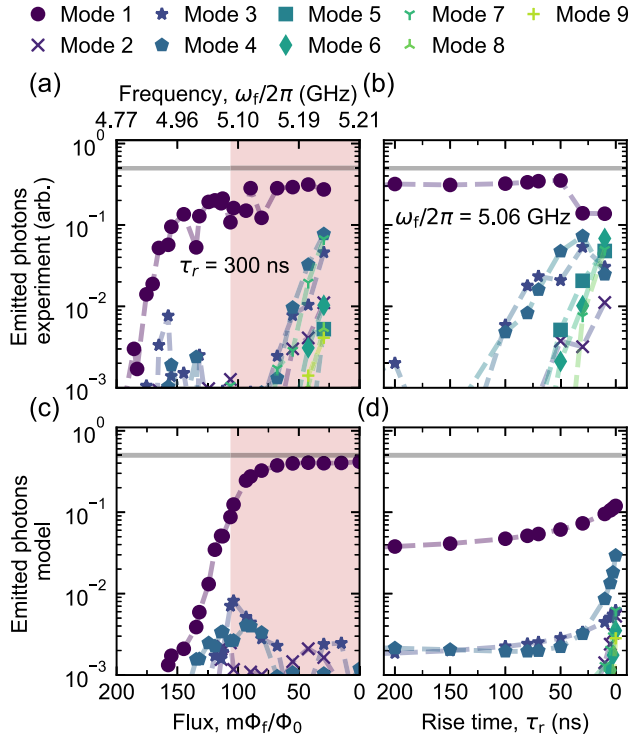


FIG. 4. Emission mode components depending on control parameters. Dashed lines connect data points for visual reference. (a) Emitted photons vs Φ_f for $\tau_r = 300$ ns. Salmon: transmission band. Data normalized so maximum emission equals 0.5 photons (horizontal gray line). (b) Emitted photons vs τ_r at $\omega_f/2\pi = 5.06$ GHz (inverted x axis). (c),(d) Numerical simulations for (a),(b).

excitation of propagating modes in the nonadiabatic regime.

Our model captures the main observed trends [Figs. 4(c) and 4(d)]. It reproduces the dominant emission from the lowest-frequency mode in the adiabatic regime [Fig. 4(c)] and the increased participation of higher-frequency modes at shorter τ_r [Fig. 4(d)]. However, there are quantitative differences. In the adiabatic regime, close to the band there are small discrepancies in the emission participation of higher-frequency modes, and, the model does not reproduce the rapid emission rise within the band [Figs. 4(a) and 4(c)]. In the nonadiabatic regime [Figs. 4(b) and 4(d)], the model predicts a shift from single-mode to multimode emission at shorter τ_r . We ascribe these differences to a combination of factors. First, the flux line's transfer function distorts flux pulses, affecting the speed at which the metamaterial modes are crossed and driving the system outside the adiabatic regime, which explains the sharp increase in participation of higher-frequency modes [Figs. 4(a) and 4(b)]. Second, measuring undercoupled edge modes requires higher power, which can shift their frequencies due to the resonator's nonlinearity and affect the model parameters. Lastly, disorder in the array may lead

to uneven couplings to the ports and nonsymmetric spatial distribution of the propagating modes, affecting the relative strength of the detected emission. These two factors explain the discrepancies in the nonmonotonic emission [Figs. 4(a) and 4(c)] (Supplemental Material [48]).

In conclusion, our Letter integrates emitter population measurements and frequency-resolved radiation detection to elucidate the dynamic interaction between a quantum emitter and a metamaterial. The finite coupling of the emitter to the modes of the metamaterial results in a speed threshold for adiabatic excitation transfer from the bare emitter to the APBS. Understanding this threshold is important for using APBS in quantum simulators, as bound states have smaller anharmonicities than the bare emitters they originate from [32,35], making adiabatic-state preparation potentially more advantageous than direct-pulsed excitation. In addition, we have directly observed the melting of an APBS following a quench of the emitter's frequency, by detecting its emitted radiation. By resolving the frequency components of the emitted radiation, we gain direct access to the spectral decomposition of the APBS into its photonic components. This method can be applied to more exotic photonic lattices, multiple bound states coupled to the same lattice, or multiphoton bound states beyond the single-excitation subspace.

Acknowledgments—We are grateful to Aamir Ali and Axel Eriksson for technical support, to Linus Andersson for fabricating the sample package, to Anita Fadavi Roudsari for her contributions to the nanofabrication recipes, to Alejandro Gonzalez-Tudela and Francesco Ciccarello for their input on the manuscript, and to Ariadna Soro and Anton Frisk Kockum for initial discussions. The Schrödinger equation was solved using QuTiP [47]. The device in this work was fabricated in Myfab, Chalmers, a micro and nanofabrication laboratory. This work received support from the Swedish Research Council and the Knut and Alice Wallenberg Foundation through the Wallenberg Center for Quantum Technology (WACQT). S.G. acknowledges financial support from the European Research Council via Grant No. 101041744 ESQuAT.

- [1] J. S. Douglas, H. Habibian, C.-L. Hung, A. V. Gorshkov, H. J. Kimble, and D. E. Chang, Quantum many-body models with cold atoms coupled to photonic crystals, *Nat. Photonics* **9**, 326 (2015).
- [2] A. Gonzalez-Tudela, C.-L. Hung, D. E. Chang, J. I. Cirac, and H. J. Kimble, Subwavelength vacuum lattices and atom-atom interactions in two-dimensional photonic crystals, *Nat. Photonics* **9**, 320 (2015).
- [3] A. Biella, L. Mazza, I. Carusotto, D. Rossini, and R. Fazio, Photon transport in a dissipative chain of nonlinear cavities, *Phys. Rev. A* **91**, 053815 (2015).
- [4] L. Lu, J. D. Joannopoulos, and M. Soljacic, Topological states in photonic systems, *Nat. Phys.* **12**, 626 (2016).

- [5] G. Calajo, F. Ciccarello, D. Chang, and P. Rabl, Atom-field dressed states in slow-light waveguide QED, *Phys. Rev. A* **93**, 033833 (2016).
- [6] V. M. Martinez Alvarez and M. D. Coutinho-Filho, Edge states in trimer lattices, *Phys. Rev. A* **99**, 013833 (2019).
- [7] R. Belyansky, S. Whitsitt, R. Lundgren, Y. Wang, A. Vrajitoarea, A. A. Houck, and A. V. Gorshkov, Frustration-induced anomalous transport and strong photon decay in waveguide QED, *Phys. Rev. Res.* **3**, L032058 (2021).
- [8] G. P. Fedorov, S. V. Remizov, D. S. Shapiro, W. V. Pogosov, E. Egorova, I. Tsitsilin, M. Andronik, A. A. Dobronosova, I. A. Rodionov, O. V. Astafiev, and A. V. Ustinov, Photon transport in a Bose-Hubbard chain of superconducting artificial atoms, *Phys. Rev. Lett.* **126**, 180503 (2021).
- [9] F. Ciccarello, Resonant atom-field interaction in large-size coupled-cavity arrays, *Phys. Rev. A* **83**, 043802 (2011).
- [10] A. S. Sheremet, M. I. Petrov, I. V. Iorsh, A. V. Poshakinskiy, and A. N. Poddubny, Waveguide quantum electrodynamics: Collective radiance and photon-photon correlations, *Rev. Mod. Phys.* **95**, 015002 (2023).
- [11] D. Fernandez-Fernandez and A. Gonzalez-Tudela, Tunable directional emission and collective dissipation with quantum metasurfaces, *Phys. Rev. Lett.* **128**, 113601 (2022).
- [12] J. Román-Roche, E. Sánchez-Burillo, and D. Zueco, Bound states in ultrastrong waveguide QED, *Phys. Rev. A* **102**, 023702 (2020).
- [13] G. Calajo, Y.-L. L. Fang, H. U. Baranger, and F. Ciccarello, Exciting a bound state in the continuum through multiphoton scattering plus delayed quantum feedback, *Phys. Rev. Lett.* **122**, 073601 (2019).
- [14] C.-L. Hung, A. Gonzalez-Tudela, J. I. Cirac, and H. J. Kimble, Quantum spin dynamics with pairwise-tunable, long-range interactions, *Proc. Natl. Acad. Sci. U.S.A.* **113**, E4946 (2016).
- [15] D. E. Chang, J. S. Douglas, A. Gonzalez-Tudela, C.-L. Hung, and H. J. Kimble, Colloquium: Quantum matter built from nanoscopic lattices of atoms and photons, *Rev. Mod. Phys.* **90**, 031002 (2018).
- [16] C. D. Bruzewicz, J. Chiaverini, R. McConnell, and J. M. Sage, Trapped-ion quantum computing: Progress and challenges, *Appl. Phys. Rev.* **6**, 021314 (2019).
- [17] A. McDonald, T. Pereg-Barnea, and A. A. Clerk, Phase-dependent chiral transport and effective non-Hermitian dynamics in a bosonic Kitaev-Majorana chain, *Phys. Rev. X* **8**, 041031 (2018).
- [18] T. Manovitz, Y. Shapira, N. Akerman, A. Stern, and R. Ozeri, Quantum simulations with complex geometries and synthetic gauge fields in a trapped ion chain, *PRX Quantum* **1**, 020303 (2020).
- [19] M. K. Joshi, A. Elben, B. Vermersch, T. Brydges, C. Maier, P. Zoller, R. Blatt, and C. F. Roos, Quantum information scrambling in a trapped-ion quantum simulator with tunable range interactions, *Phys. Rev. Lett.* **124**, 240505 (2020).
- [20] I. Carusotto, A. A. Houck, A. J. Kollar, P. Roushan, D. I. Schuster, and J. Simon, Photonic materials in circuit quantum electrodynamics, *Nat. Phys.* **16**, 268 (2020).
- [21] J. D. Brehm, A. N. Poddubny, A. Stehli, T. Wolz, H. Rotzinger, and A. V. Ustinov, Waveguide bandgap engineering with an array of superconducting qubits, *npj Quantum Mater.* **6**, 1 (2021).
- [22] M. Mirhosseini, E. Kim, V. S. Ferreira, M. Kalae, A. Sipahigil, A. J. Keller, and O. Painter, Superconducting metamaterials for waveguide quantum electrodynamics, *Nat. Commun.* **9**, 3706 (2018).
- [23] A. Vrajitoarea, R. Belyansky, R. Lundgren, S. Whitsitt, A. V. Gorshkov, and A. A. Houck, Ultrastrong light-matter interaction in a multimode photonic crystal, [arXiv:2209.14972](https://arxiv.org/abs/2209.14972).
- [24] A. Morvan *et al.*, Formation of robust bound states of interacting microwave photons, *Nature (London)* **612**, 240 (2022).
- [25] M. Bello, G. Platero, and A. Gonzalez-Tudela, Spin many-body phases in standard- and topological-waveguide QED simulators, *PRX Quantum* **3**, 010336 (2022).
- [26] X. Zhang, E. Kim, D. K. Mark, S. Choi, and O. Painter, A scalable superconducting quantum simulator with long-range connectivity based on a photonic bandgap metamaterial, *Science* **379**, 278 (2023).
- [27] C. Tabares, A. Munoz de las Heras, L. Tagliacozzo, D. Porras, and A. Gonzalez-Tudela, Variational quantum simulators based on waveguide QED, *Phys. Rev. Lett.* **131**, 073602 (2023).
- [28] T. McBroom-Carroll, A. Schlaves, X. Xu, J. Ku, B. Cole, S. Indrajeet, M. D. LaHaye, M. H. Ansari, and B. L. T. Plourde, Entangling interactions between artificial atoms mediated by a multimode left-handed superconducting ring resonator, *PRX Quantum* **5**, 020325 (2024).
- [29] V. S. Ferreira, G. Kim, A. Butler, H. Pichler, and O. Painter, Deterministic generation of multidimensional photonic cluster states with a single quantum emitter, *Nat. Phys.* **20**, 865 (2024).
- [30] V. D. Vaidya, Y. Guo, R. M. Kroeze, K. E. Ballantine, A. J. Kollar, J. Keeling, and B. L. Lev, Tunable-range, photon-mediated atomic interactions in multimode cavity QED, *Phys. Rev. X* **8**, 011002 (2018).
- [31] Y. Liu and A. A. Houck, Quantum electrodynamics near a photonic bandgap, *Nat. Phys.* **13**, 48 (2016).
- [32] N. M. Sundaresan, R. Lundgren, G. Zhu, A. V. Gorshkov, and A. A. Houck, Interacting qubit-photon bound states with superconducting circuits, *Phys. Rev. X* **9**, 011021 (2019).
- [33] E. Kim, X. Zhang, V. S. Ferreira, J. Banker, J. K. Iverson, A. Sipahigil, M. Bello, A. Gonzalez-Tudela, M. Mirhosseini, and O. Painter, Quantum electrodynamics in a topological waveguide, *Phys. Rev. X* **11**, 011015 (2021).
- [34] V. S. Ferreira, J. Banker, A. Sipahigil, M. H. Matheny, A. J. Keller, E. Kim, M. Mirhosseini, and O. Painter, Collapse and revival of an artificial atom coupled to a structured photonic reservoir, *Phys. Rev. X* **11**, 041043 (2021).
- [35] M. Scigliuzzo, G. Calajo, F. Ciccarello, D. Perez Lozano, A. Bengtsson, P. Scarlino, A. Wallraff, D. Chang, P. Delsing, and S. Gasparinetti, Controlling atom-photon bound states in an array of Josephson-junction resonators, *Phys. Rev. X* **12**, 031036 (2022).
- [36] C. Vega, D. Porras, and A. Gonzalez-Tudela, Topological multimode waveguide QED, *Phys. Rev. Res.* **5**, 023031 (2023).

- [37] J. Koch, T. M. Yu, J. Gambetta, A. A. Houck, D. I. Schuster, J. Majer, A. Blais, M. H. Devoret, S. M. Girvin, and R. J. Schoelkopf, Charge-insensitive qubit design derived from the Cooper pair box, *Phys. Rev. A* **76**, 042319 (2007).
- [38] P. Krantz, M. Kjaergaard, F. Yan, T. P. Orlando, S. Gustavsson, and W. D. Oliver, A quantum engineer's guide to superconducting qubits, *Appl. Phys. Rev.* **6**, 021318 (2019).
- [39] A. Blais, A. L. Grimsmo, S. M. Girvin, and A. Wallraff, Circuit quantum electrodynamics, *Rev. Mod. Phys.* **93**, 025005 (2021).
- [40] M. D. Hutchings, J. B. Hertzberg, Y. Liu, N. T. Bronn, G. A. Keefe, M. Brink, J. M. Chow, and B. L. T. Plourde, Tunable superconducting qubits with flux-independent coherence, *Phys. Rev. Appl.* **8**, 044003 (2017).
- [41] F. Lombardo, F. Ciccarello, and G. M. Palma, Photon localization versus population trapping in a coupled-cavity array, *Phys. Rev. A* **89**, 053826 (2014).
- [42] A. V. Shytov, Landau-Zener transitions in a multilevel system: An exact result, *Phys. Rev. A* **70**, 052708 (2004).
- [43] K. Saito, M. Wubs, S. Kohler, Y. Kayanuma, and P. Hanggi, Dissipative Landau-Zener transitions of a qubit: Bath-specific and universal behavior, *Phys. Rev. B* **75**, 214308 (2007).
- [44] A. Stehli, J. D. Brehm, T. Wolz, A. Schneider, H. Rotzinger, M. Weides, and A. V. Ustinov, Quantum emulation of the transient dynamics in the multistate Landau-Zener model, *npj Quantum Inf.* **9**, 1 (2023).
- [45] M. Wubs, K. Saito, S. Kohler, P. Hanggi, and Y. Kayanuma, Gauging a quantum heat bath with dissipative Landau-Zener transitions, *Phys. Rev. Lett.* **97**, 200404 (2006).
- [46] M. A. Rol, L. Ciorciaro, F. K. Malinowski, B. M. Tarasinski, R. E. Sagastizabal, C. C. Bultink, Y. Salathe, N. Haandbaek, J. Sedivy, and L. DiCarlo, Time-domain characterization and correction of on-chip distortion of control pulses in a quantum processor, *Appl. Phys. Lett.* **116**, 054001 (2020).
- [47] J. R. Johansson, P. D. Nation, and F. Nori, QuTiP 2: A Python framework for the dynamics of open quantum systems, *Comput. Phys. Commun.* **184**, 1234 (2013).
- [48] See Supplemental Material at <http://link.aps.org/supplemental/10.1103/PhysRevLett.134.133601>, which includes Refs. [49–56], for additional information about the experimental methods and the used models.
- [49] N. A. Masluk, I. M. Pop, A. Kamal, Z. K. Mineev, and M. H. Devoret, Microwave characterization of Josephson junction arrays: Implementing a low loss superinductance, *Phys. Rev. Lett.* **109**, 137002 (2012).
- [50] P. V. Klimov *et al.*, Fluctuations of energy-relaxation times in superconducting qubits, *Phys. Rev. Lett.* **121**, 090502 (2018).
- [51] J. J. Burnett, A. Bengtsson, M. Scigliuzzo, D. Niepce, M. Kudra, P. Delsing, and J. Bylander, Decoherence benchmarking of superconducting qubits, *npj Quantum Inf.* **5**, 1 (2019).
- [52] J. Lisenfeld, A. Bilmes, A. Megrant, R. Barends, J. Kelly, P. Klimov, G. Weiss, J. M. Martinis, and A. V. Ustinov, Electric field spectroscopy of material defects in transmon qubits, *npj Quantum Inf.* **5**, 1 (2019).
- [53] A. Bilmes, A. Megrant, P. Klimov, G. Weiss, J. M. Martinis, A. V. Ustinov, and J. Lisenfeld, Resolving the positions of defects in superconducting quantum bits, *Sci. Rep.* **10**, 3090 (2020).
- [54] M. A. Rol, F. Battistel, F. K. Malinowski, C. C. Bultink, B. M. Tarasinski, R. Vollmer, N. Haider, N. Muthusubramanian, A. Bruno, B. M. Terhal, and L. DiCarlo, Fast, high-fidelity conditional-phase gate exploiting leakage interference in weakly anharmonic superconducting qubits, *Phys. Rev. Lett.* **123**, 120502 (2019).
- [55] M. Jerger, A. Kulikov, Z. Vasselin, and A. Fedorov, In situ characterization of qubit control lines: A qubit as a vector network analyzer, *Phys. Rev. Lett.* **123**, 150501 (2019).
- [56] Y. Sung, L. Ding, J. Braumüller, A. Vepsäläinen, B. Kannan, M. Kjaergaard, A. Greene, G. O. Samach, C. McNally, D. Kim, A. Melville, B. M. Niedzielski, M. E. Schwartz, J. L. Yoder, T. P. Orlando, S. Gustavsson, and W. D. Oliver, Realization of high-fidelity CZ and zz-free iSWAP gates with a tunable coupler, *Phys. Rev. X* **11**, 021058 (2021).